



Flow regime transitions for Aiding flow around a heated cylinder: A numerical and experimental investigation

C.W. Hollingshead^{a,*}, A. Rashkovan^b, D.R. Novog^a

^a Department of Engineering Physics, McMaster University, Hamilton, Ontario, Canada

^b Nuclear Research Center Negev (NRCN), Beer-Sheva 84190, Israel



ABSTRACT

Experiments and numerical simulations were performed to examine the interplay between buoyancy and momentum effects for mixed convection flow around a 13.4 mm diameter cylinder in water. PIV and LIF measurements were made to obtain experimental velocity and temperatures over a *Ri* range from 0 to 9. LES models were validated against the measured experimental conditions and then used to numerically study the parametric behaviour over a wider range of conditions. The CFD model was found to perform well, with a small tendency to over predict temperature and velocity measurements for higher buoyancy conditions, *Ri* > 1.9. Using the experimental LIF results, three flow regimes around the cylinder were identified, grouped, and made into a flow regime map. From this, two sets of transition criteria were developed and proposed to predict the collapse of the recirculation zone and the total suppression of vortex formation. This was done via observations from the experimental data and additional CFD simulations to examine the separate effects of fluid properties and incident turbulence levels, both of which were shown to influence vortex suppression significantly. The criteria proposed was found to accurately capture the visually observed flow regimes experimentally in water.

$$Re_D = \frac{\rho v_\infty D}{\mu} \quad (2)$$

$$Ri = \frac{Gr}{Re^2} = \frac{g\beta\Delta TD}{v_\infty^2} \quad (3)$$

1. Introduction

Cylinders are the foundational building block of industrial heat exchangers and have a presence in Nuclear Reactor components, such as the horizontal calandria tubes in the moderator of a CANDU reactor. Whilst flow around an adiabatic cylinder has been extensively studied, comparatively less has been done on heated cylinders. Specifically on how the convective and buoyant forces interact, and how the local conditions (temperature, velocity) in mixed convection affect the observed phenomena such as heat transfer. Design shifts in Generation IV reactors has led to passive safety features to enhance safety, utilizing natural and mixed convection. As such, adding more experimental and modelling efforts to the mixed and natural convection regime has become more important. The relative strength of buoyancy and momentum can be characterized by the Richardson number (*Ri*) as shown in Eq. (3) below and is a function of both *Re* and *Gr*. Generally, forced convection dominates for *Ri* < 0.1, and natural convection above *Ri* > 10 (Cengel, 2002). The region in-between being referred to as Mixed Convection where both effects are present and contribute to heat transfer.

$$Gr_D = \frac{g\beta\Delta TD^3}{\nu^2} \quad (1)$$

An important phenomenon identified in the literature related to mixed convective flows around cylinders is the disappearance of von-Karman Vortices at some critical *Ri*. Above the critical *Ri* the flow field transitions to a “thermally dominated” regime, which is more stable and begins to behave similarly to that of a free thermal plume. Below this critical transition, von-Karman Vortices are observed. This transition has been explored experimentally by studies such as (Hu and Koochesfahani, 2011; Lecordier et al., 1991; Lecordier et al., 2000; Khashehchi et al., 2015; Michaux-Leblond and Belorgey, 1997; Singh et al., 2007; Kakade et al., 2010) with relevant experimental studies summarized in Table 1 with notable differences being observed between experiments with water and air.

The study of Michaux-Leblond and Belorgey (1997) experimentally examined the wake behind a 11.7 mm diameter cylinder in water. Using Laser Doppler Velocimetry, it was determined that at a *Ri* of 0.49 a transition occurred and the vortex sheet typically observed for flow around a cylinder was suppressed. When this suppression was first reached, it was found that two simultaneous and approximately symmetric eddies were observed. As heating power was increased further, a secondary flow developed and filled in the momentum deficit region of

* Corresponding author.

E-mail address: hollincw@mcmaster.ca (C.W. Hollingshead).

Nomenclature	
PIV	Particle Image Velocimetry
LIF	Laser Induced Fluorescence
CFD	Computational Fluid Dynamics
LES	Large Eddy Simulation
<i>Gr</i>	Grashof Number
<i>Ri</i>	Richardson Number
<i>Re</i>	Reynolds Number
<i>Pr</i>	Prandtl Number
<i>St</i>	Strouhal Number
<i>C_{pb}</i>	Base Pressure Coefficient
<i>k</i>	Thermal Conductivity [W/mK]
β	Volumetric thermal expansion coefficient [1/K]
<i>c_p</i>	Specific Heat Capacity [J/kgK]
μ	Dynamic Viscosity[Pas]
\dot{m}	Mass Flow Rate [kg/s]
<i>v</i>	Kinematic viscosity [m ² /s]
v_{∞}	Average Inlet Velocity [m/s]
<i>D</i>	Diameter of vessel [m]
<i>L</i>	Length of vessel/heater rods [m]
<i>g</i>	Acceleration due to gravity [m/s ²]
<i>T_w</i>	Cylinder Wall Temperature [K]
<i>T_{in}</i>	Nozzle Inlet temperature [K]
<i>T_i</i>	Inlet Turbulent Intensity
<i>q''</i>	Heat flux [W/m ² K]
<i>Q</i>	Heater Power [W]

the wake and suppressed the formation of the two eddies entirely. [Hu and Koochesfahani \(2011\)](#) studied the wake of a heated cylinder in opposed flow. Velocity and temperature fields as a function of *Ri* were measured employing molecular tagging velocimetry and thermometry in water, respectively. Using a copper tube with a 4.76 mm diameter in a working fluid of water it was found that below *Ri* = 0.31, no change to the von-Karman vortices was observed. For the values of *Ri* between 0.31 and 0.72, it was noted that von-Karman vortices appear to be delayed and began further downstream from the cylinder as compared with the adiabatic case. At *Ri* > 0.72, the von-Karman vortices were replaced by smaller wake vortices, generated symmetrically on both sides of the cylinder, and were noted to contain more of a Kelvin-Helmholtz type nature.

[Singh et al. \(2007\)](#) examined the suppression of vortices for circular and square cylinders in air via Schlieren interferometry. It was reported that above a certain *Ri*, vortices were entirely precluded from forming with no mention of a symmetric wake vortices shedding process that were obtained for water (see [\(Hu and Koochesfahani, 2011; Michaux-Leblond and Belorgey, 1997\)](#)). This critical *Ri* was noted to be similar for the circular and square cases and was dependent on *Re*, with higher *Re* yielding higher critical *Ri*. The wake behind a square cylinder using Schlieren interferometry at variety of *Re* and orientations was also examined by [Kakade et al. \(2010\)](#). The general increase in critical *Ri* with increasing *Re* reported by [Singh et al. \(2007\)](#) was confirmed. Additionally, when the square cylinder side walls were aligned with the flow path, the critical *Ri* was minimized. The critical *Ri* was maximized when the angle was increased to 20° and held constant to an angle of 45° (the maximum angle employed). This was suggested to be a result of an increase in the adverse pressure gradient caused by the edges of the square channel. [Khashechi et al. \(2015\)](#) experimentally examined the wake behind a cylinder in a wind tunnel for a *Ri* in the range of 0 to 0.22 for a cross-flow orientation. No change was observed to the classical von-Karman shedding flow topology for *Ri* up to 0.05. Above *Ri* of 0.05, an asymmetry driven by buoyancy began to exist with the upper vortex distorted upwards compared to the adiabatic case. From both experimental studies in air, there was a lack of the transition vortex symmetric shedding phenomena that was observed in water.

Numerical studies of the phenomena in mixed convection over a

circular cylinder have also been conducted including ([Singh et al., 1998; Chang and Sa, 1990; Wan and Patnaik, 2016; Gandikota et al., 2010; Singh and Chandar, 2016](#)). [Singh et al. \(1998\)](#) and [Chang and Sa \(1990\)](#) numerically investigated the forced to free convection transition in air at a *Re* of 100, and both found a critical *Ri* of 0.15. As opposed to the experimental observations in air of [Singh et al. \(1998\)](#), the transition in the numerical work involved the generation of symmetric eddy pairs. The study of [Wan and Patnaik \(2016\)](#) numerically examined the suppression of vortex induced vibrations in cylinders solely by thermal effects using their own code. Using simulations with a cylinder connected to a spring in a channel in a cross-flow, it was noted that as the power to the cylinder was increased in the range of *Ri* between 0.1 and 0.2, very little changed in the flow structures around the cylinder, except for a gradual narrowing of the vortex street. For *Ri* greater than 0.3, no vortices were detected. Increasing further the *Ri*, they found a critical *Ri* of 0.8, above which all vibrations were fully suppressed. Additionally, this critical *Ri* was found to be dependent on the free stream velocity.

Previous studies on adiabatic flow around a circular cylinder, such as the one by [Feng and Wang \(2010\)](#) experimentally demonstrated in water that the pure von-Karman shedding processes can be interrupted and replaced by a symmetric shedding mode when momentum is introduced into the wake region via jets. The experiments of [Fu and Rockwell \(2005\)](#) introduced a slit parallel to the flow direction into the cylinder and varied this slit size using water as the working fluid. They found that for increasing slit size, the von-Karman shedding process was shifted away from the cylinder. Additionally, when the slit reached a critical size (for a fixed *Re*), the rear-wake region of the cylinder appeared to be divided into two separate symmetric regions. [Gao et al. \(2017\)](#) also examined the effects of a parallel slit size in a cylinder experimentally in air. Similarly to [Fu and Rockwell \(2005\)](#), [Gao et al. \(2017\)](#) reported that above a certain size, symmetric vortices begin to compete with the regular von-Karman shedding mode, suppressing the central recirculation zone and appearing to split it into two recirculation zones. These effects were also observed and studied in the experiments of [Shi and Feng \(2015\)](#). Examining the parallel slit geometry numerically, [Baek and Karniadakis \(2009\)](#) showed similar results to the experimental studies discussed above. Additionally, it was found that the symmetric vortices shedding process began at a smaller slit size for an inlet *Re* of

Table 1

Shows the critical *Ri* from studies in literature.

Study	Cylinder Diameter [mm]	Working Fluid	Flow Orientation	Re range	Ri Range	Ri ² crit quoted
Hu and Koochesfahani, 2011	4.76	Water	Opposing	135	0–1.04	0.72
Michaux-Leblond and Belorgey, 1997	11.7	Water	Aiding	130–327	0–4	0.49
Khashechi et al., 2015	30	Air	Cross	1000–4000	0–0.2	N/A
Singh et al., 2007	6.2	Air	Aiding	85–92	0–0.18	0.122–0.157

² The *Ri*_{crit} quoted in these experiments are not consistent and can refer to different phenomena.

1000 as compared to Re of 500. This change in slit size required to introduce the symmetric shedding mode suggests a dependency on the base pressure coefficient of the cylinder. Studies such as Williamson and Roshko (1990) have also shown the decrease of rear-base pressure coefficient with Re in the range examined by Baek and Karniadakis (2009), which may partially explain the reduced slit size required in this Re range. This division of the re-circulation zone also appears to be occurring in heated experiments with momentum induced via buoyancy effects replacing the bypassed flow from the adiabatic slit experiments as evidenced by observations from Hu and Koochesfahani (2011) and Michaux-Leblond and Belorgey (1997). This phenomenon is further examined in this study.

The goal of the present study is to conduct new experimental and numerical analysis to better understand the underlying phenomena behind the transitions observed in mixed convection flows around a heated cylinder. This was done via PIV and LIF measurements over a Ri range from 0 up to 9, which significantly expands the range of Ri compared to that presently available in literature. This study also proposes transition criteria to classify flow regimes around a heated cylinder as a function of Ri . Finally, this criteria is used and expanded upon via LES to help explain the different flow phenomena observed between experiments using air and water. More specifically, to explain why a paired eddy shedding mode exists for experiments using water, and appears to not exist in experiments in air, such as Singh et al. (2007).

2. Experimental setup and conditions

The aim of the current experimental study was to examine how the inlet velocity and power supplied to a cylinder impact the flow fields around a horizontal cylinder in the mixed convective Ri regime. To achieve the experimental goals, two separate experimental campaigns were performed.

- Particle Image Velocimetry for velocity measurements
- Laser Induced Fluorescence for fluid temperature measurements

The geometry consisted of a horizontal cylindrical test vessel which was 489.3 mm in diameter by 504.7 mm in length as used in Hollingshead et al. (2022) – seen in Fig. 1 (left). The heater used was the same Heater A as described in Hollingshead et al. (2022). This heater had a diameter of 13.4 mm and was un-instrumented with the electrical connections on one side to allow for ideal optical access. The heat flux shape was a cosine shape with a heated length of 500 mm. Note that all measurements presented are for the central region in the peak heat flux of the heater.

2.1. Nozzle/inlet condition

To adequately control the inlet velocity a 3-D printed nozzle was designed and built. The design was based by CFD calculations employing the $k-\omega$ SST turbulence model – with the cut-view in Fig. 1 (right). The $k-\omega$ SST turbulence model was used due to its ability to capture salient flow features for early prototypes built and examined via PIV. The velocity profile of the nozzle was measured for a variety of flow rates and can be seen below on Fig. 2 with tabulated time and space averaged values shown in Table 2. It should be noted that the flow field outside the nozzle as measured employing the PIV camera system was found to be asymmetrically positioned under the heater with a shift of 6 mm. This asymmetry was not correctable due to positioning errors in the assembly of the end plates of the vessel, in addition to potential manufacturing errors in the positioning of the inlet and outlet ports to the vessel. This asymmetry was accounted for in subsequent CFD simulations. Tables 3A and 3B.

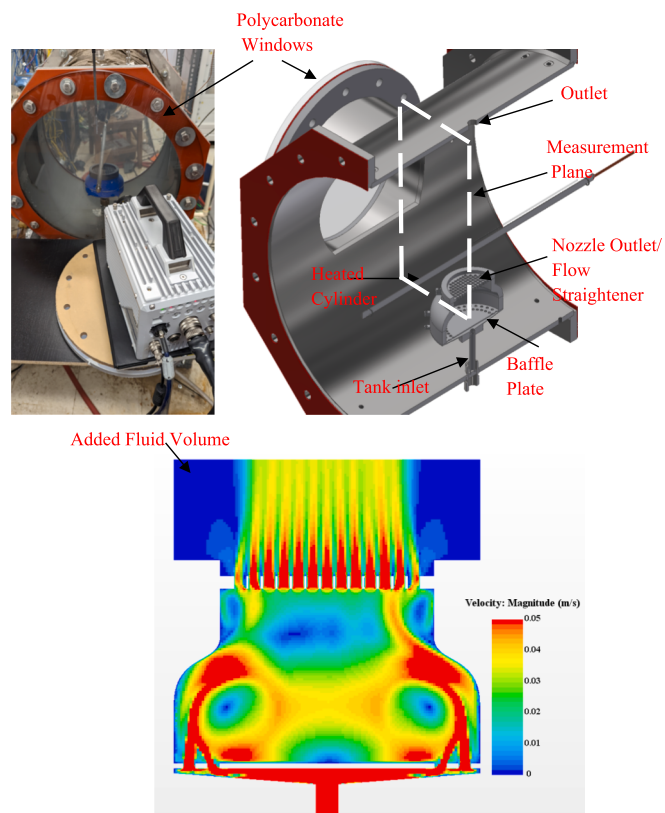


Fig. 1. The test section with the nozzle at the bottom of the vessel just below the heater with the PIV/LIF camera in view (left), an isometric drawing of the test section (right) and an instantaneous velocity magnitude contour on a symmetry plane of the diffuser nozzle simulations at 100 g/s (bottom).

2.2. Particle Image Velocimetry

The PIV experiments were performed using a Photron SA5 highspeed camera and a ND-YLF pulsed laser. The camera and laser were synchronized via a synchronizer which was set to a capture frequency of 125 Hz and a laser pulse delay of 7800 μ s for a typical pixel displacement of 1–5 pixels. Due to camera buffer limitations, five sets of 400 image pairs were captured for a total time averaging time of 20 s. This was used to obtain the time averaged velocity fields. Additionally, the camera was placed on a 10-degree tilt from the imaging plane, as this was found to significantly help with the quality of heated measurements in Hollingshead et al. (2022). Adiabatic tests were done with and without this 10-degree tilt, which showed no impact on the velocity field in the regions reported.

The uncertainty in the PIV measurements was assessed to be 3 mm/s via repeatability measurements. This was to account for errors in camera positioning, laser sheet alignment, and process system variability. Additional uncertainty due to pixel displacement (~ 0.1 pixel) was not included as it was found to be much smaller than the 3 mm/s. The laser sheet thickness was approximately 3 mm, indicating that all velocity measurements are averaged over this volume.

2.3. Laser induced fluorescence

To clearly observe the thermal plumes and measure the local plume temperatures Rhodamine B dye was added to the water at a concentration of approximately 1.2×10^{-7} mol/L. The LIF measurement procedure, including a 10-degree camera tilt, closely follows the one outlined in Hollingshead et al. (2022). Since LIF measurements do not require laser-camera coincident timing, the camera and laser were not synchronized for these measurements to avoid the camera buffer errors

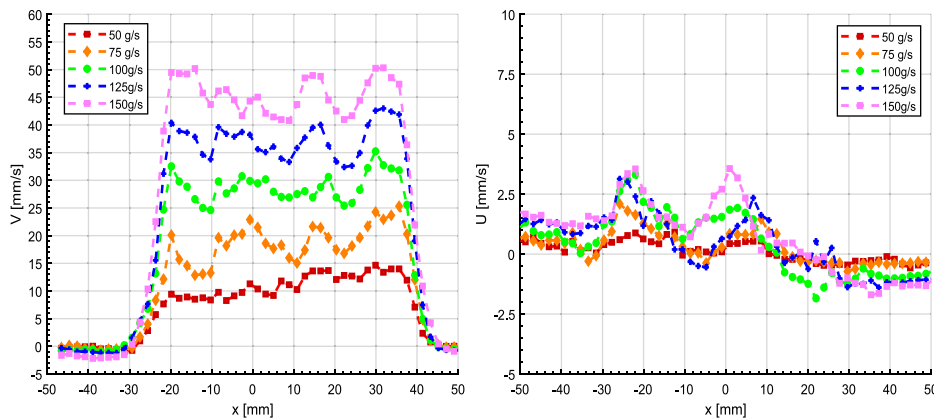


Fig. 2. PIV velocity (vertical, left and horizontal, right) profiles measured 20 mm below the cylinder for isothermal conditions (note $x = 0$ mm corresponds to the centre of the heater rod).

Table 2
Nozzle time-averaged parameters versus mass flow.

Inlet Flow Rate (g/s)	Measured Average Velocity (mm/s)	Turbulent Intensity	Re
50±1	12.4±3	0.2 ±40	187
75±1	18.3±3	0.34 ±40	275
100±1	27.5±3	0.27 ±40	414
125±1	35.5±3	0.3 ±40	534
150±1	44.2±3	0.31 ±40	665

Table 3A
Experimental Conditions in Dimensional and Non-Dimensional Form.

Inlet Flow Rate [g/s]	Re	Heater Power [W]	Gr
50	207	145	1.13×10^5
50	222	270	2.40×10^5
50	248	512	5.60×10^5
75	303	145	9.85×10^5
75	324	270	2.10×10^5
75	340	384	3.31×10^5
75	358	512	4.91×10^5
75	376	640	6.78×10^5
100	449	145	8.36×10^5
100	479	270	1.78×10^5
100	501	384	2.79×10^5
100	527	512	4.15×10^5
100	550	640	5.70×10^5
100	575	768	7.52×10^5
100	597	896	9.53×10^5
125	576	145	7.46×10^4
125	611	270	1.58×10^5
125	639	384	2.48×10^5
125	669	512	3.67×10^5
125	698	640	5.04×10^5
125	727	768	6.62×10^5
125	755	896	8.43×10^5
150	713	145	6.74×10^4
150	753	270	1.42×10^5
150	786	384	2.22×10^5
150	821	512	3.28×10^5
150	856	640	4.50×10^5
150	889	768	5.89×10^5
150	923	896	7.50×10^5

Table 3B
Critical Richardson number vs Pr via varying other fluid properties.

Pr_∞	Parameter Modified	Ri_C Observed via LES	Equation (7)
2	$c_p = 1409 \text{ J/kgK}$	0.48 ± 0.08	0.444
2	$\mu = 3 \times 10^{-4} \text{ Pa s}$ (Re held constant)	0.45 ± 0.06	0.444
15	$c_p = 10,472 \text{ J/kgK}$	1.9 ± 0.2	1.89
15	$k = 0.249 \text{ W/mK}$	2.0 ± 0.2	1.89

mentioned above for the PIV measurements. The laser was operating at a frequency of 1000 Hz with the camera at a capture frequency of 125 Hz and shutter frequency of 1000 Hz. These setting was found to minimize intensity fluctuations in the images.

The error in the LIF temperature measurements was evaluated to be 1.1°C . This was assessed via a contribution of the measured standard deviation in the intensity of a flat temperature field of approximately 1 % converted to a temperature and the error in the type T thermocouple used for calibration. Repeatability measurements were also performed but were found to agree well within this 1.1°C error and as such did not contribute to the total error. This improvement in repeatability performance compared to the PIV measurements was directly attributed to the improvement in laser sheet visibility. This was a direct result of the fluorescence of the Rhodamine B.

Sample images from the LIF measurements can be seen in Fig. 3 for a variety of inlet flow rates at a fixed power. The change in flow topology vs flow rate is quite noticeable. Starting at 75 g/s and 512 W, the flow topology appears to largely resemble that of a free thermal plume, qualitatively containing more disturbances than a free thermal plume due to velocity difference between the plume and the small but still significant convective components. As the flow rate is increased to 100 g/s, the plume width increases and the length scale of the disturbances appears to increase, though the nature of the disturbances appear to be the same as the 75 g/s case. Increasing this flow rate further to 125 g/s, the width increased further, and coincident eddies began shedding from the cylinder. Additionally, there no longer appeared to be a contiguous region of hot fluid from the top of the heater to the end of the measurement window as seen for the more thermal 75 and 100 g/s cases. When the flow is increased to 150 g/s, the width of the rear-wake region is largely unchanged. However, the shedding mode changes, and instead of simultaneous shedding they become alternating, appearing to be classic asymmetrically shedding von-Karman vortices.

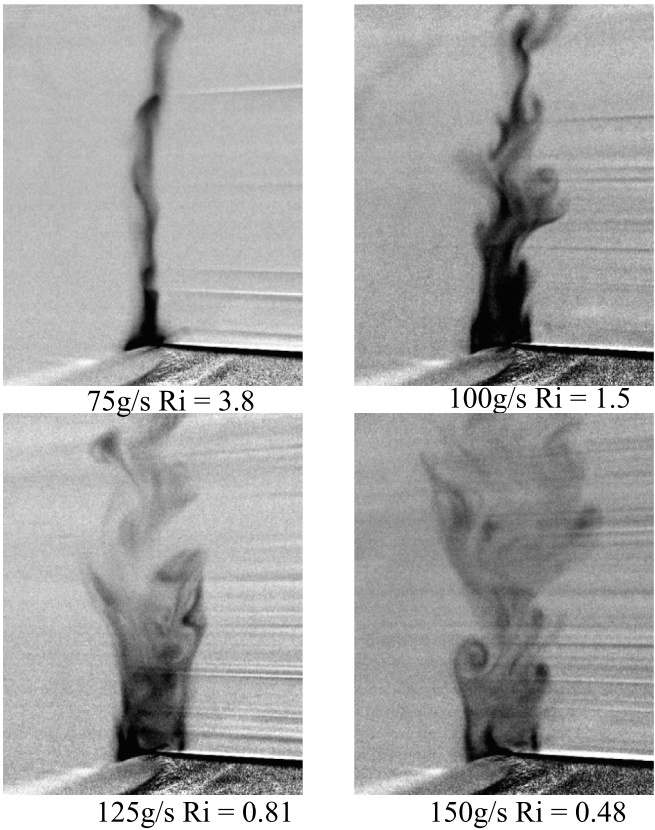


Fig. 3. LIF instantaneous intensity fields measured for four mass flow rates at a power of 512 W.

3. Experimental results

3.1. Velocity measurements

Selected PIV results showing time-average vertical velocity can be seen in Fig. 4 and Fig. 5. These figures show the downstream contours of the wake for increasing heat input. A gradual narrowing and eventual disappearance of recirculation zone downstream of the cylinder,¹ in Fig. 4, is observed as the heater power is increased. This is indicative of a transition to buoyancy dominated flow, and the suppression of the von Karman vortex street. This is further illustrated in Fig. 5 which shows that for a variety of flow/power combinations the negative velocity in the recirculation zone vanishes for higher ratios of the input powers (buoyancy force) to mass flow rate (momentum). Additionally, as it follows from Fig. 5(b and d), as the power level is increased, a change in curvature is present in the region $0.5 < Y/D < 1.5$. This change is believed to be associated with an increasing buoyant force and the development of a thermal plume in the flow field.

3.2. Fluid temperature measurements

Time averaged measurements of local fluid temperature difference relative to the inlet are presented in Fig. 6 for a variety of cylinder power levels and inlet flow rates. As the inlet power is increased for a fixed flow rate, there is a gradual thinning of the wake region and an increase in the temperature, indicating the development of a thermal plume. This is consistent with the velocity measurements presented in Fig. 5 which also indicate that the region downstream the cylinder becomes more buoyant

in nature. Transient videos and phenomena discussed in subsequent sections also indicate that as the power is increased, or the flow decreased at a fixed power, fewer disturbances are visible in the flow field. This is attributed to the added momentum due to the buoyancy in the wake region. The effect of this thought to increase the average velocity in the wake region. This decreases the velocity gradient across the wake and reduces the primary mode of turbulence generation.

3.3. Flow regime map

Three regimes were identified to classify the wakes with characteristics observed. These were von Karman vortices (VKV), eddy pair (EP) and thermal dominated flow as identified on Fig. 7. Given the unique changes in the turbulent behaviour in the wake of a tube in mixed convection flow observations were collected over a wide range of Gr , Re and Ri . To organize the data and to narrow the focus for subsequent analyzes, a flow regime map was created based in the experimental observations. The map was based on visual observations from videos generated by the LIF transient data and is presented in Fig. 8. Additionally, several lines of constant Ri are plotted to highlight the range of Ri conditions measured.

3.3.1. von Karman vortices regime

The experiments had an inlet Re in the 200 to 700 range as shown by Table 2. This range corresponds to boundary of the Transition-in-Wake (TrW) and the Transition in Shear Layers (TrSL) regimes as classified by Zdravkovich (1997). The effects of inlet turbulence intensity on the TrW regime were examined by Aarnes et al. (2018) up to 25 % via DNS simulations. Aarnes et al. (2018) found that the Strouhal number of this regime decreased slightly at an inlet turbulent intensity of 25 % versus none. This indicates that for the current study, the shedding frequencies may be slightly smaller than correlations would predict. Additionally, the lower range of Re in this study has been examined numerically by Rajani et al. (2009).

The von-Karman vortices regime, or VKV, is characterized by the traditional von Karman vortex street associated with the TrSL regime visualized in Fig. 7 (top left). At these ranges of conditions (blue crosses in Fig. 8), the flow field around the heated cylinder is very similar to that of an adiabatic case. This regime of flow around an adiabatic cylinder is largely characterized by one vortex shedding after another in an alternating fashion. As power is increased, the length and width of the recirculation zone behind the cylinder monotonically decreases as seen in Fig. 9 with little change to the vortex shedding process until the recirculation zone collapses and the Eddy Pair regime discussed in section 4.3.2 is reached. As the power is increased, in the near field at the top of the cylinder, what will be referred to as a precursor plume begins to form. The precursor plume is the hot fluid at the top of the cylinder that forms but is unable to rise from the cylinder surface. This appears to be a result of negative recirculation pressure holding back this hot fluid. This precursor plume tends to wobble from side to side, shedding with the vortices as they are generated from whichever side the precursor plume is currently on. Per the experimental observations of Fu and Rockwell (2005), Gao et al. (2017) and Shi and Feng (2015), the transition to the next regime likely occurs when this precursor plume becomes strong enough to divide the momentum boundary layer of the cylinder, with a buoyant plume replacing the physical jets in their adiabatic experiments.

3.3.2. Eddy pair regime

Once the heat input reaches a certain power level, the fluid on top of the cylinder contains enough buoyancy to partially counteract the recirculating fluid. This appears to alter the vortex shedding process as the vortices begin to shed nearly simultaneously on both sides of the cylinder, as seen in Fig. 7 (top right). The precursor plume continues to grow and oscillate from side to side as in the previous VKV regime, except in this case oscillations occur with the simultaneous eddy pair.

¹ The recirculation zone is characterized experimentally as the region of fluid where negative average vertical velocity values are obtained.

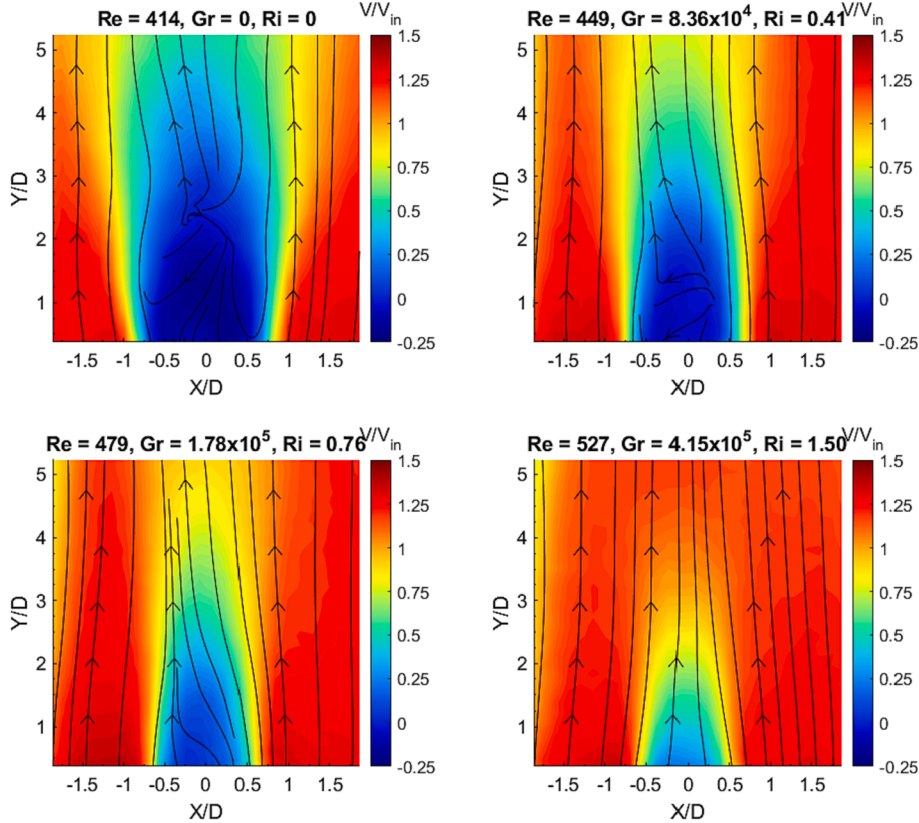


Fig. 4. PIV results of the wake behind the cylinder as a function of Gr (time averaged contours) for a fixed inlet mass flow rate of 100 g/s. Note, $Y/D = 0$ corresponds to the top of the cylinder surface.

However the precursor plume is still confined to the wake of the cylinder, though it appears to be larger than at lower powers.

Power Spectral Density (PSD) analysis at the 125 g/s flow rate taken at the point $X/D = 0$, $Y/D = 5.22$ is shown in Fig. 10. The transition from VKV regime appears to increase the St from 0.20 to approximately 0.25. This increase is attributed to changing dynamic viscosity and density with increasing power, increasing the local Re . Additionally, the increase could be partially due to the vortices no longer getting “dragged” towards the rear of the cylinder before shedding. This may allow for a subtle increase in shedding frequency and the St . As the PSD analysis was performed on the LIF data due to the lack of camera buffer issues, no adiabatic data was possible and the direct effect of the turbulent intensity on the shedding frequency was also not available. Though, expanding the general trend backward towards zero power would appear to yield a slight decrease in St , which would be consistent with the predictions of Aarnes et al. (2018) for the effect of inlet turbulent intensity on shedding frequency.

The pairwise eddy shedding appears to continue until the buoyant force becomes strong enough to entirely force all fluid in the near-cylinder wake region upward, completely overcoming the recirculation flows that are driving vortex generation. It should be noted that in the experiments of Singh et al. (2007) and Kakade et al. (2010) for air, this regime was not observed. This indicates that property differences between air and water appears to be significantly affect regime transition.

3.3.3. Thermal regime

The thermal regime is a broad classification and is first reached when vortices no longer form, or form very infrequently due to occasional disturbances. The size of the plume in this regime varies greatly, from being near the size of the diameter of the cylinder when first reached to approximately the thickness of a free thermal plume. This is partially

visualized in Fig. 9, showing the gradual thinning on the wake region vs Ri which shows that around a Ri of 4, that the width of the plume/wake region no longer shrinks. Around this Ri , it is considered to have the flow topology of a free thermal plume.

4. LES modelling

To study the transitions further, obtain more data, and assess the phenomenological differences between fluids, LES modelling of the flows was performed using STAR-CCM+. The computational domain used can be seen below in Fig. 11. The domain was 7 cylinder diameters long and 489.3 mm in total diameter. The outlet was a 19 mm diameter opening at the top of the vessel and in the centre of the domain. The walls of the domain were no-slip walls and a 60 mm diameter cut-out was placed 20 mm below the cylinder spanning the length of the nozzle to simulate the inlet nozzle. The circular cut out for the inlet condition was offset by 6 mm to account for the small asymmetry between the jet and cylinder in the experiments. The inlet velocity boundary condition for the nozzle was matched to the experimentally obtained inlet velocity distributions. The synthetic turbulence on the inlet for the LES simulations was inputted with the turbulent intensity of a given experimental condition with a length scale of 5 mm, the diameter of the inlet flow straightener. To handle buoyancy effects the Boussinesq approximation was used. The wall was modelled via the all $y+$ wall model.

As was stated previously, the present study spans from the upper transition in wake regime (TrW) to lower subcritical transition in shear layer (TrSL), following Zdravkovich (1997) classification of the regimes of flow around the circular cylinder. Of numerous studies on LES modelling of the flow around the circular cylinder in regimes relevant to the present study, including e.g. Rajani et al. (2016) in TrSL and Xiyun and Guocan (2002) for the Re characteristic of transition from TrW to TrSL regime, it can be concluded that the dynamic Smagorinsky model is

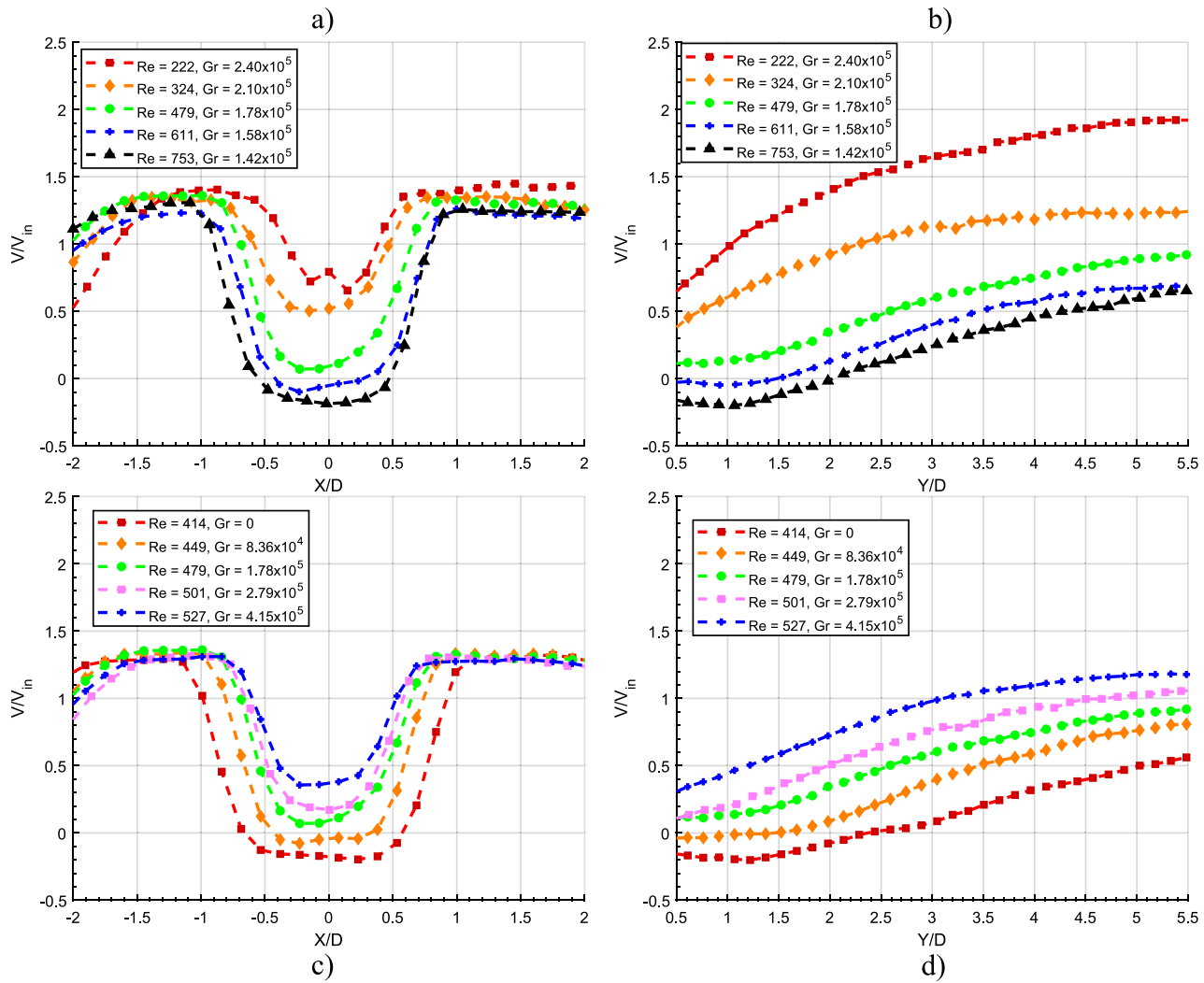


Fig. 5. Vertical velocity profile for $Y/D = 0.746$ away from the cylinder surface (left) and the centreline $X/D = 0$ velocities (right). Note, a) and b) correspond to a fixed heater power and c) and d) a fixed inlet flow rate.

capable of capturing the flow phenomena for the conditions employed in the present study. Furthermore, the simulations of Clifford and Kimber (2020) showed exceptional performance of the dynamic Smagorinsky model for natural convection flows in a square cavity.

4.1. Sensitivities

To ensure the CFD fidelity sensitivity to mesh, timestep and turbulent intensity on the inlet conditions were examined for the 100 g/s adiabatic condition. It should be noted that these were performed after ensuring that the computational model was capable of handling >95 % of the turbulent kinetic energy, as confirmed by applying the Large-Eddy Simulation Quality Index (LESIQ) proposed by Celik et al. (2005) to the domain. This criteria suggests that LES simulations are of good quality since >80 % of the energy containing eddies are captured by the mesh and temporal resolution of the simulation (Celik et al., 2005). In general, little sensitivity to mesh and timestep was noted, as seen in Fig. 12 below. Owing to this, a mesh base size of 1 mm and timestep of 0.1 s were chosen for the 100 g/s or 27.5 mm/s inlet velocity case. For other flow rates, the timestep was varied to assure a maximum CFL value of approximately 3. Over a ±5 % window of the turbulent intensity from the experimentally measured values, no significant difference in velocity profiles was obtained. Additionally, the maximum y^+ on the cylinder wall was found to be 1.8, indicating a proper resolving of the boundary

layer. Another sensitivity study was performed for a mesh very similar to the one employed in this study for free thermal plumes in the work of Hollingshead et al. (2022) which also showed little sensitivity to mesh or timestep.

4.2. Validation

To validate the LES modelling a wide range of experimental conditions were chosen covering a Ri range from 0 to 1.9. These ranges of conditions were also chosen to have validation cases for each flow regime identified. The choice of including an adiabatic condition was made to help isolate modelling errors in either the momentum or buoyant fields. This data can be seen in Fig. 13, with each plot containing all the experimental measurements against CFD predictions in the measurement window. Note, to ensure alignment of the data, the data is interpolated onto the same grid, so each point in a plot on Fig. 13 corresponds to a comparison between CFD and experiment at a position.

4.2.1. VKV regime validation: $Re = 414, Gr = 0$ and $Re = 449, Gr = 8.36 \times 10^4$

The general performance of the model for the VKV regime can be seen below in Fig. 13a). The strong performance of the thermal field would appear to largely be due to the very small temperature gradients in relation to the error in the LIF measurements of 1.1 °C. The

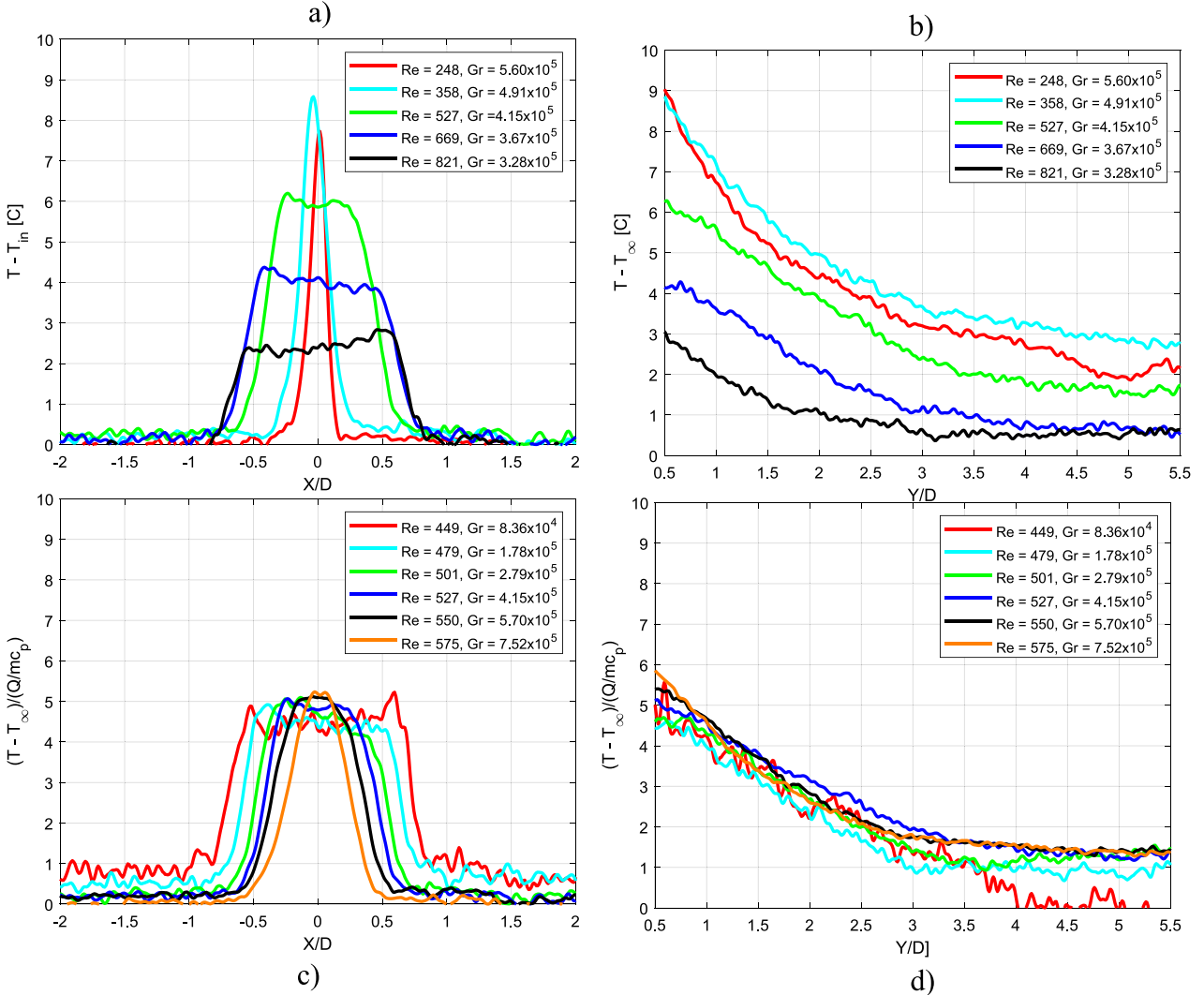


Fig. 6. Temperature profiles for a variety of conditions at $Y/D = 0.37$ above the cylinder a) and c), and the centreline profiles away from the cylinder b) and d). Plots a) and b) correspond to a fixed power, and c) and d) correspond to a fixed inlet flow rate.

performance in the velocity field for the model however is mixed with conflicting indicators. The RMS error indicates a good performing model, yielding a value of 2.31 mm/s compared to the measurement uncertainty of 3 mm/s. However, this measurement uncertainty captures only 80 % of the total predictions. When the added systematic error introduced into the simulations via the inlet condition uncertainty is accounted for, by increasing these error bounds to 5 mm/s, 96.4 % of the predictions are covered. Additionally, when examining the velocity profiles for the $Re = 414$ case in Fig. 14, good agreement is found with nearly all data points lying within measurement error. This level of agreement appears to be consistent with the study of Rajani et al. (2016) and Xiyun and Guocan (2002).

4.2.2. EP regime validation: $Re = 479, Gr = 1.78 \times 10^5$

The performance of the EP regime predictions can be seen in Fig. 13b). The thermal performance for this regime was exceptional, with all the data lying within measurement uncertainty. The performance of the velocity predictions was less so, with only 72.2 % of predictions within 3 mm/s. This increases to 85 % if the bars are expanded to 5 mm/s. The main driver for this reduced performance appears to largely be due to a slight difference in slope in the sharp gradient in the $0.5 < |X/D| < 1$ region, which appears to occur over a smaller distance than the VKV regime as evidenced by Fig. 14b). The performance of this

model in this regime is considered to be strong aside from this region, nearly all data along the centreline agreeing with experiment as shown in Fig. 14b). This is further evidenced by an RMS error of 3.28 mm/s, slightly error than the measurement error. Additionally, the predicted temperature field agrees very well with experiment as shown in Fig. 15b).

4.2.3. Thermal regime validation: $Re = 527, Gr = 4.15 \times 10^5$ and $Re = 324, Gr = 2.10 \times 10^5$

As the flow topology becomes increasing thermal, performance characteristics identified by Ma and He (2021) and also seen in Hollingshead et al. (2022) become apparent. Ma and He (2021) found that for LES simulations for natural convection around a circular cylinder there was a tendency to over-predict velocities by 15 % and under predict Nu relative to experiment. In Fig. 13c) and d), the model begins to over predict the local temperatures relative to the experimental results. This level of over-prediction appears to be worse with increasing buoyancy, the lower Re case tending to over predict the centreline temperature by 2 °C as compared to the higher Re case as seen in Fig. 15c) and d). Conversely, the level of performance in the velocity predictions appears to be consistent with that of the EP regime, with the velocity predictions largely covered by measurement uncertainty in Fig. 14. For the most buoyant condition examined, $Ri = 1.90$, in the far

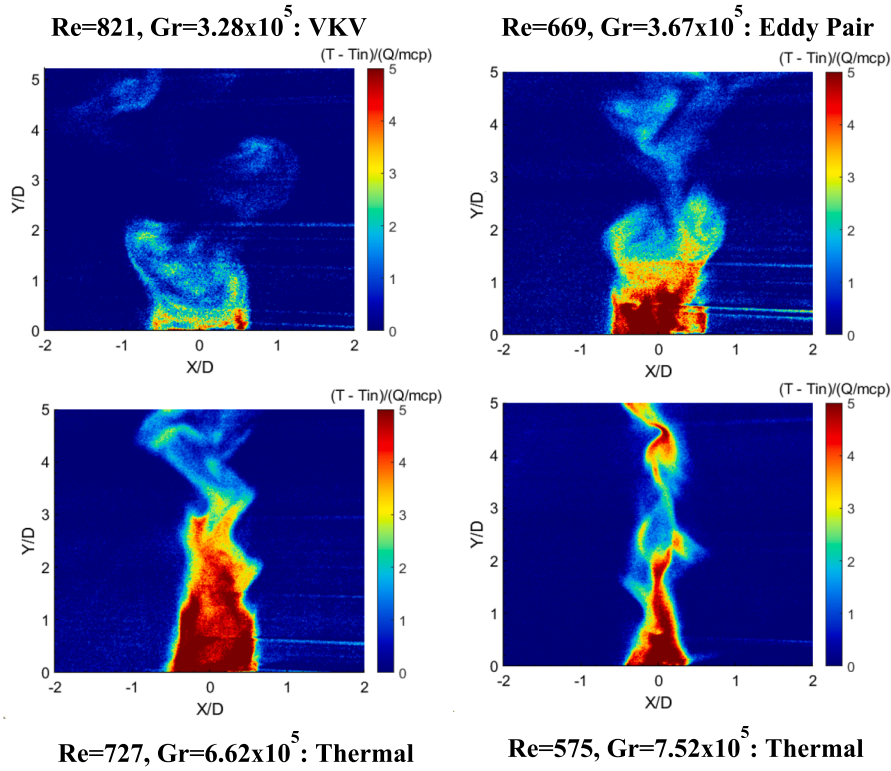


Fig. 7. Normalized instantaneous temperature profiles identifying each of the three regimes observed.

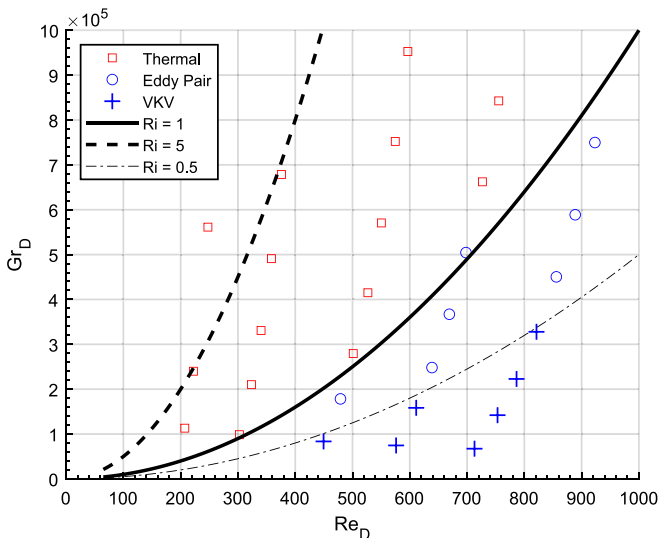


Fig. 8. Flow regime map of experimental data points with lines of constant Ri to indicate approximate buoyancy to force convective strengths.

field of Fig. 14d) (left), there appears to be the beginning of an over-prediction of the velocity field. This systematic over-prediction is consistent with the results shown by Ma and He (2021), and is suspected to get worse with increasing Ri past this point.

The underlying cause of this apparent over-prediction of buoyancy may result from a combination of the models slight deficiency in predicting the heat transfer and/or issues in the SGS model for highly buoyant conditions. In terms of heat transfer, the under prediction of Nu as shown by Ma and He (2021) may be a contributing factor. This over estimation of wall temperature would yield stronger temperature gradients in the near wall region, as evidenced by the over-prediction of

fluid temperatures and velocity predictions for $Ri = 1.90$. Conversely, Clifford and Kimber (2020) show their LES model is quite capable of capturing the Nu and show no significant deviation in their velocity predictions as compared to experiment. This puzzling difference in model performance may in part be due to the relative size difference between the characteristic lengths in those studies, and subsequently higher local heat fluxes/larger gradient magnitudes over smaller distances in the study from Ma and He (2021). Clifford and Kimber (2020) and Ma and He (2021) both used the Dynamic Smagorinsky SGS model, indicating that the difference in performance may be related to geometry scale. This is visible in the characteristic length, being 750 mm for Clifford and Kimber (2020), 54 mm for Ma and He (2021) and 13.4 mm in the present study. Given the excellent performance at large scales in the work of Clifford and Kimber (2020), this seems to suggest that under smaller scale flows the performance may deteriorate somewhat. This would appear to be an underprediction of local turbulence and spreading of thermal plumes, yielding higher temperatures and velocities relative to experiment in works such as Ma and He (2021) and Hollingshead et al. (2022).

5. Regime transitions

5.1. von-Karman vortices to eddy Pair regime

The destruction of the pure von Karman vortex sheet is proposed to be a result of the buoyant force at the top of the cylinder reaching a point where it is sufficiently strong to counteract the low pressures in the recirculation region. This would be analogous to the slit size in the experiments of Gao et al. (2017), Fu and Rockwell (2005) and Shi and Feng (2015) being large enough to allow sufficient amount of flow through the slit to counteract the suction pressure, which showed a similar transition. This results in a separation of the wake of the cylinder into two re-circulation zones and the transformation of alternating von Karman vortices into symmetric eddy pairs.

This transition is derived by considering the case where the suction

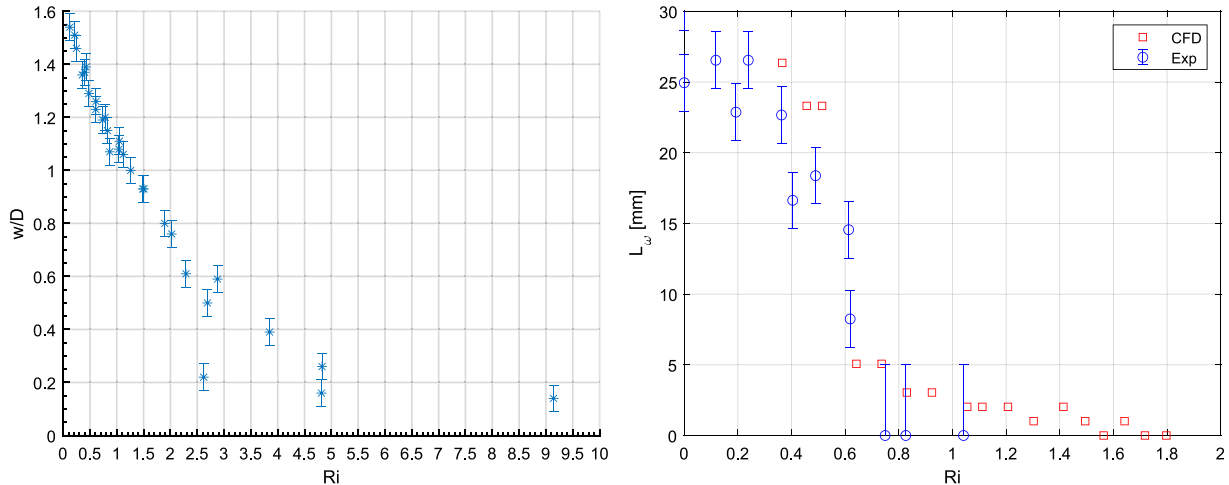


Fig. 9. Width of the thermal wake/plume region at 5 mm from the cylinder surface (left) and the length of the recirculation zone as a function of Ri (right). Note the CFD simulations are for an inlet Re of 414.

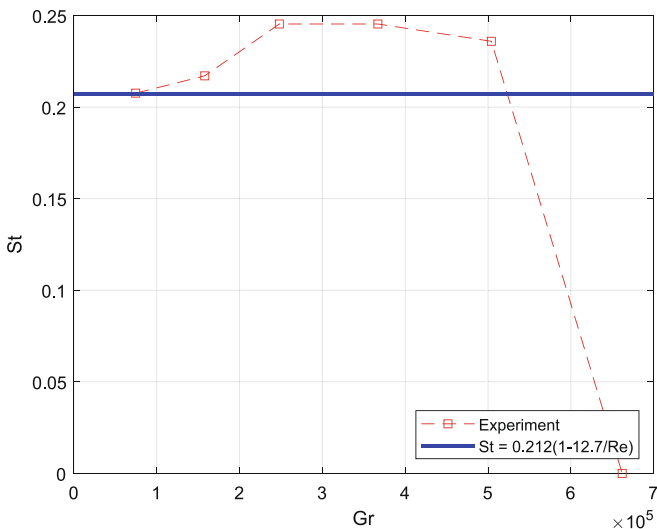


Fig. 10. Strouhal number measured from LIF data at 125 g/s as a function of heater power versus a correlation for St via Zdravkovich, 1997.

pressure in the wake of the cylinder is approximately equal to the upward buoyant force in the rear of the cylinder, as shown in equation (4). Expanding upon this formulation, using the average wall temperature difference in estimating the buoyant force equation (4) is transformed into equation (5). Equation (5) is then re-arranged into equation (6), yielding a critical Ri of half the base pressure coefficient. For the Re range of experiments conducted, the base pressure coefficient varies from 0.7 to 0.95 as shown by Williamson and Roshko (1990) and Norberg (1994). Following the proposed model (equations. (4)–(6)), this indicates that pure von Karman vortices should disappear around a Ri of 0.35 to 0.425. The force balance approach to the destruction of the von Karman vortices is expected to correspond with the collapse of the recirculation zone in the centre region as it begins to be divided by buoyancy, which can be seen on Fig. 9 (right) to occur in $0.5 < Ri < 0.6$ region, slightly delayed compared to the prediction of the criteria. This is thought to be attributed to the relatively high turbulent intensity measured on the inlet condition and is further details addressed in section 6.4 below. It should be repeated that the Eddy Pair regime has not been observed in experiments using air such as Singh et al. (2007).

$$F_{suction} = F_\beta \quad (4)$$

$$\frac{C_{pb}}{2} \rho V_\infty^2 A \approx \rho g \beta \Delta T_w D A \quad (5)$$

$$Ri_{T1} = \frac{C_{pb}}{2} \quad (6)$$

5.2. Eddy Pair to thermal regime

The transition from the eddy pair regime to the thermal regime is proposed to be the point whereby buoyancy and buoyant induced flow is strong enough in the entire upper portion of the cylinder to counteract the suction pressure in the momentum boundary layer of the cylinder. This is partially confirmed by the observations of Singh et al. (2007), who noted an increase in the measured critical Ri as a function of Re . One can suggest that this would indicate that the critical Ri for this regime is dependent on the base pressure coefficient C_{pb} , which via a force balance would yield a Ri of $C_{pb}/2$, as before. The use of C_{pb} is justified by experimental studies by Achenbach (1968), which show the pressure coefficient to be almost uniform over the downstream half of the cylinder. The value of C_{pb} was obtained from a lookup table generated from the experimental data of Norberg (1994) and Williamson and Roshko (1990) for a wide range of Re .

As noted prior, the EP regime has not been observed in experimental studies such as Singh et al. (2007). As such the transition for total vortex suppression appears to be different, as partially visible by the significant difference in the critical Ri for air found by Singh et al. (2007) (0.122–0.157) compared to water (0.9–1.18) of the present study. There would appear to be a dependency on fluid properties which allows for air to require relatively less buoyant force to completely preclude all eddy formation. The physical rationale for this large difference is thought to be the difference in the ratio of the thermal boundary layer to the momentum boundary layer thicknesses for air and water and is examined further below.

For water at 25 °C, the thermal boundary layer is approximately half the thickness of the momentum boundary layer. This means that except for the top portion of the cylinder where the thermal boundary layer flow begins to move upward, the added buoyancy around the cylinder is unable to counteract all of the negative pressure gradient in the momentum boundary layer. While the negative pressure region is divided along the tube centerline by the thermal plume, regions of negative pressure persist on either side. This mechanism is similar to the observations of Fu and Rockwell (2005) who explored cylinder wake control in isothermal flow and beginning of phenomena identified as the “Eddy Pair” regime here. This regime would then continue until the induced buoyant velocity is strong enough to counteract the negative pressure

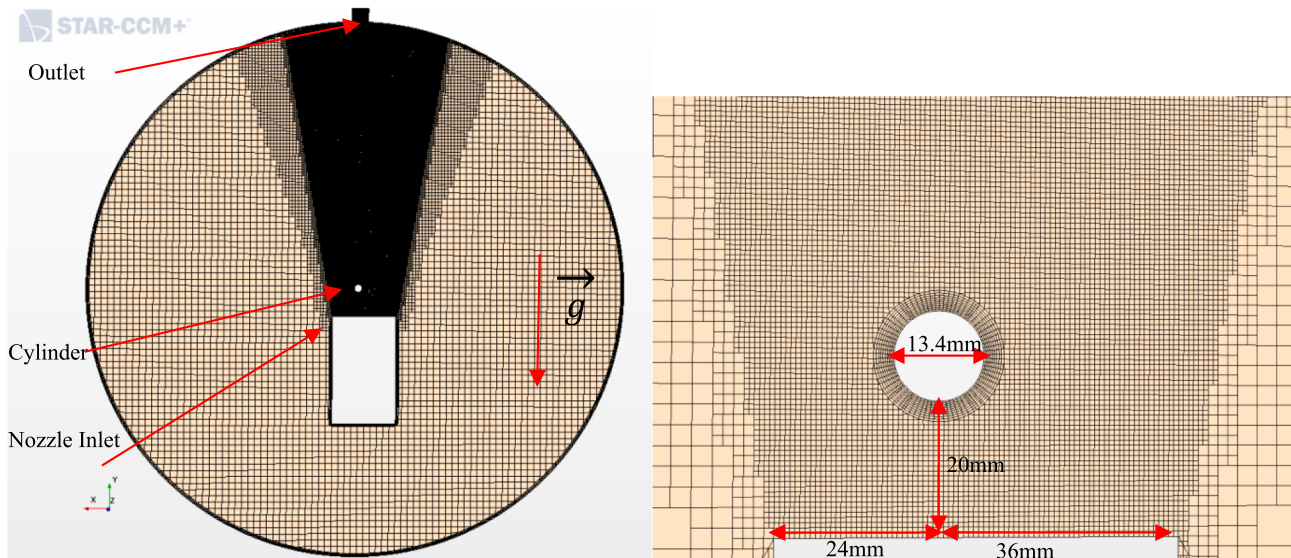


Fig. 11. Mesh cross-section for the entire domain and a zoomed in section around the heater.

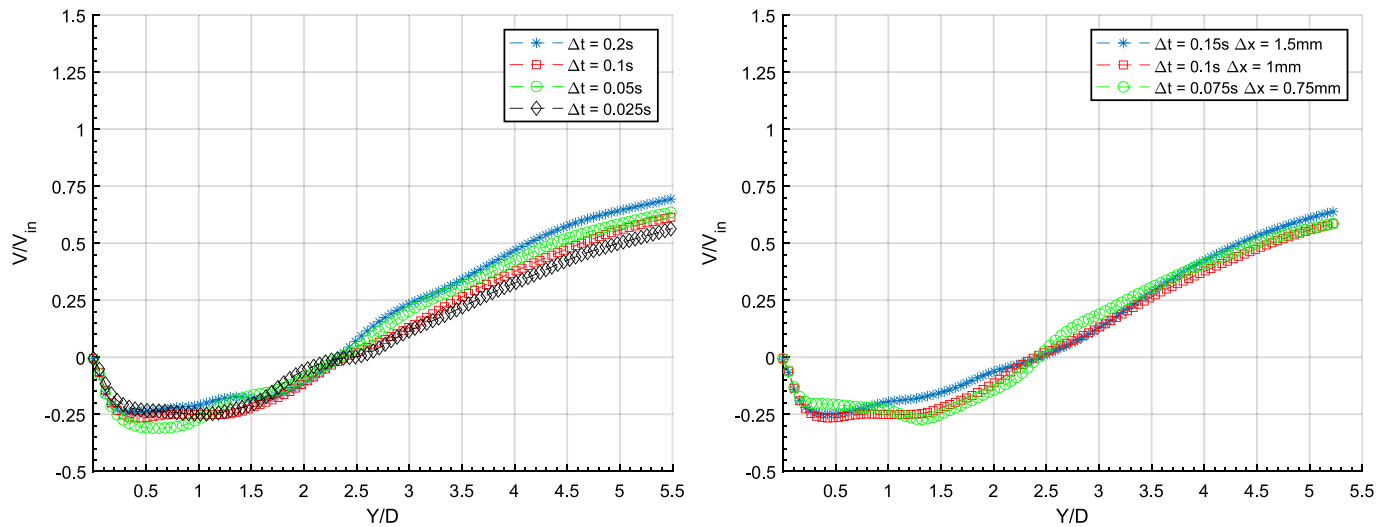


Fig. 12. Sensitivity to mesh and timestep for $Re = 414$, $Gr = 0$.

gradients in the remaining recirculation regions via shear, leading to the thermal regime. It can be suggested that for fluids with thermal boundary layers appreciably thinner than the momentum boundary layers, three flow regimes exist instead of two for the flow around a cylinder based on buoyant strength: von-Karman Vortices, Eddy Pair and Thermal as found in this study for water.

For air, the thermal and momentum boundary layers are roughly the same thickness. The key difference this implies is that the buoyancy of the thermal boundary layer is now able to act on the entire momentum boundary layer. This means that when the buoyancy force is strong enough to match the suction pressure in one region of the boundary layer, it happens in the entire boundary layer. This causes a direct transition from a VKV regime to a thermal regime, skipping the EP regime observed in the present study for water. The VKV to thermal transition is consistent with the observations of [Singh et al. \(2007\)](#).

To examine this phenomena further and over a wide range of Pr , several Pr were chosen varying from 0.7 to 50 for additional LES simulations. These simulations were performed at power level and flows that bracket the suppression point of vortices. To isolate one fluid property at a time, the modification in Pr was achieved by adjusting the

specific heat capacity of water to achieve the desired Pr . All other fluid properties were left constant, to create a fictitious fluid with a different specific heat capacity and all other properties of water constant at 25 °C. Table 3 shows similar results are obtained when other fluid properties are modified. The geometry was modified to remove the 6 mm asymmetry as noted above and the inlet turbulent intensity was reduced from 27 % to 1 %. This was to be inline with typical experiments in literature and to remove/minimize the turbulent intensity contribution. To remove Re dependencies, all simulations were performed at an inlet velocity of 27.5 mm/s, corresponding to Re of approximately 414. The resulting Ri_C obtained from observing the LES flow regimes are presented in [Fig. 16](#) with the proposed transition criteria being equation (7). Note, this is correlated to the Pr of the bulk fluid.

$$Ri_{T2} = \frac{C_{pb}}{2} (0.568 Pr^{0.719}) \quad (7)$$

5.3. Effect of inlet turbulent intensity

The transition criteria based on the above analysis tended to predict regime transitions at a lower Ri than what was observed experimentally,

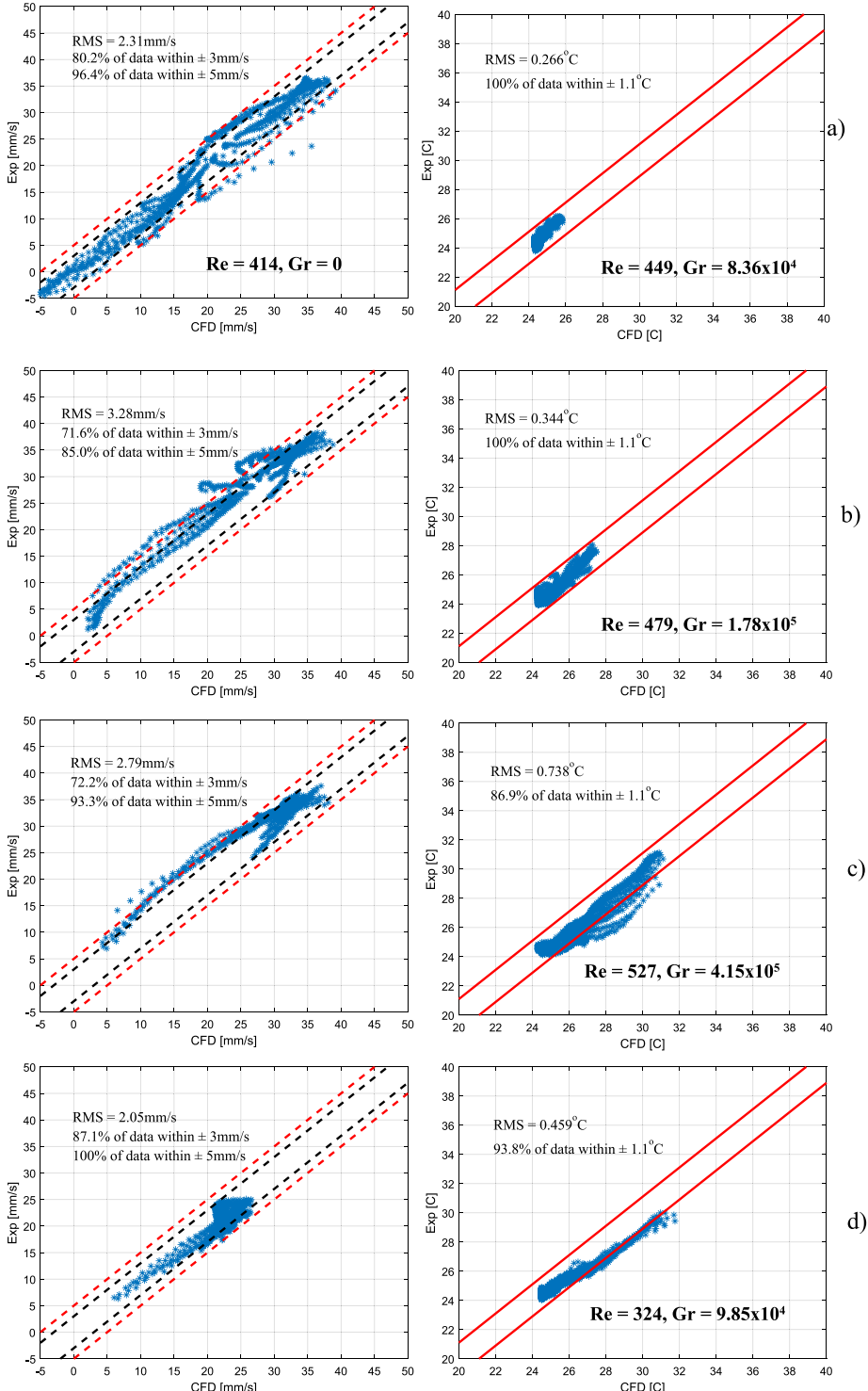


Fig. 13. Validation plots for velocity and temperature predictions: Solid red $\pm 1.1^\circ\text{C}$, dashed red $\pm 5 \text{ mm/s}$ and dashed black $\pm 3 \text{ mm/s}$. (For interpretation of the references to colour in this figure legend, the reader is referred to the web version of this article.)

especially for the VKV to EP transition while indications showed better agreement for the limited data in literature. Given the nozzle designed for these experiments yields high inlet turbulent intensities compared to these previous studies (20–30 % compared to 1 %), its effect on flow topology and regime transitions was briefly explored. Fig. 17 shows the comparison of two non-dimensional temperature snap shots from LES simulations at the same mass flow/power combination, with and without the inlet turbulent intensity for a Ri of approximately 1. The case with lower inlet turbulent intensity is much more stable and

resembles the thermal regime. Whereas the case with higher inlet turbulence intensity shows shedding-like behaviour. This appears to suggest that the added turbulent intensity extends the VKV and EP regime transitions. This would likely be due to the added disturbances, requiring a higher buoyant force to fully suppress them.

In an attempt to account for the effect of upstream turbulence intensity on the regime transitions, a simple multiplier was added to the transition criteria as shown below in equations (8)–(9). The addition of this multiplier appears to more accurately capture the flow regimes

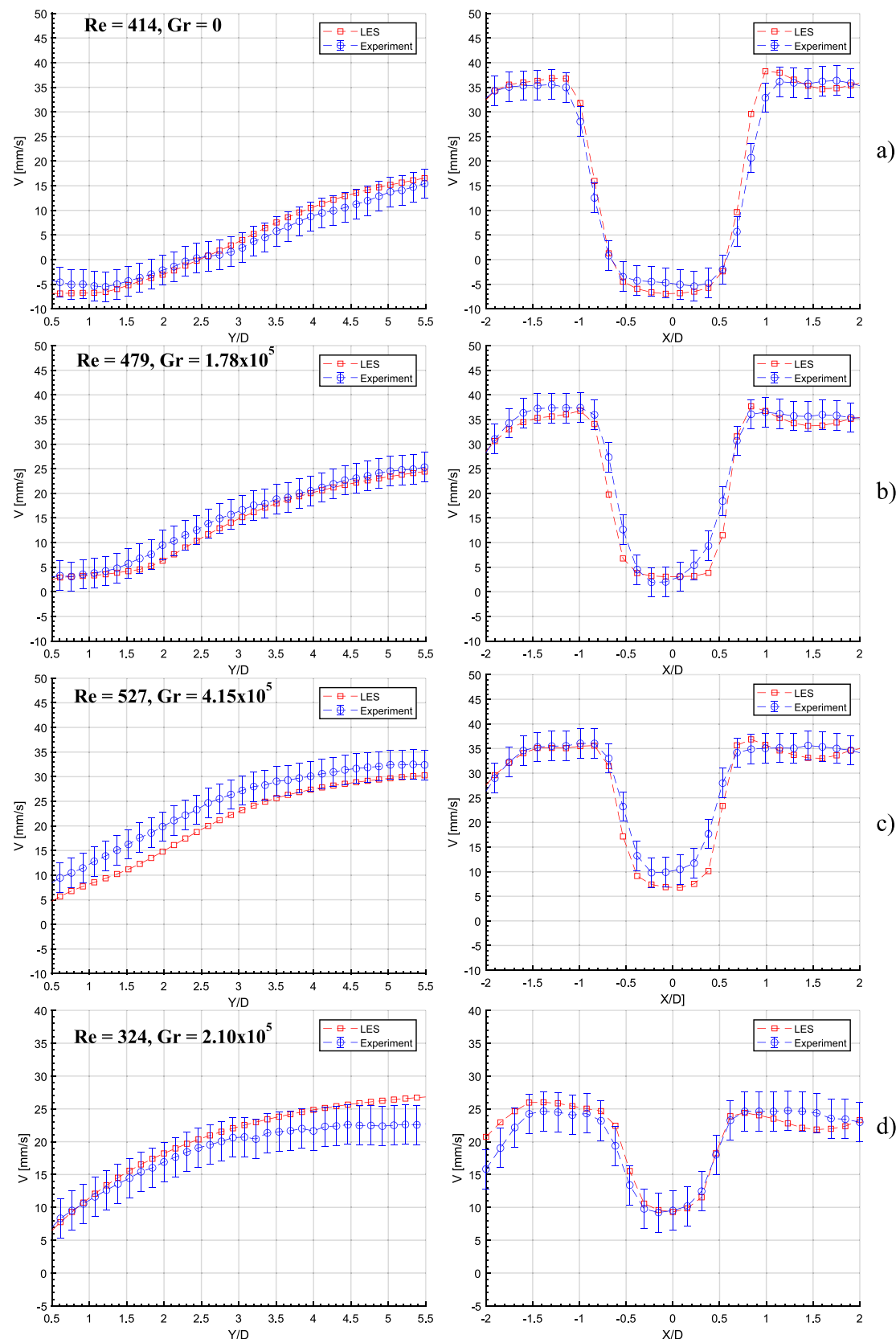


Fig. 14. Measured versus predicted velocity profiles for the lines at X/D (left) and $Y/D = 0.746$ (right).

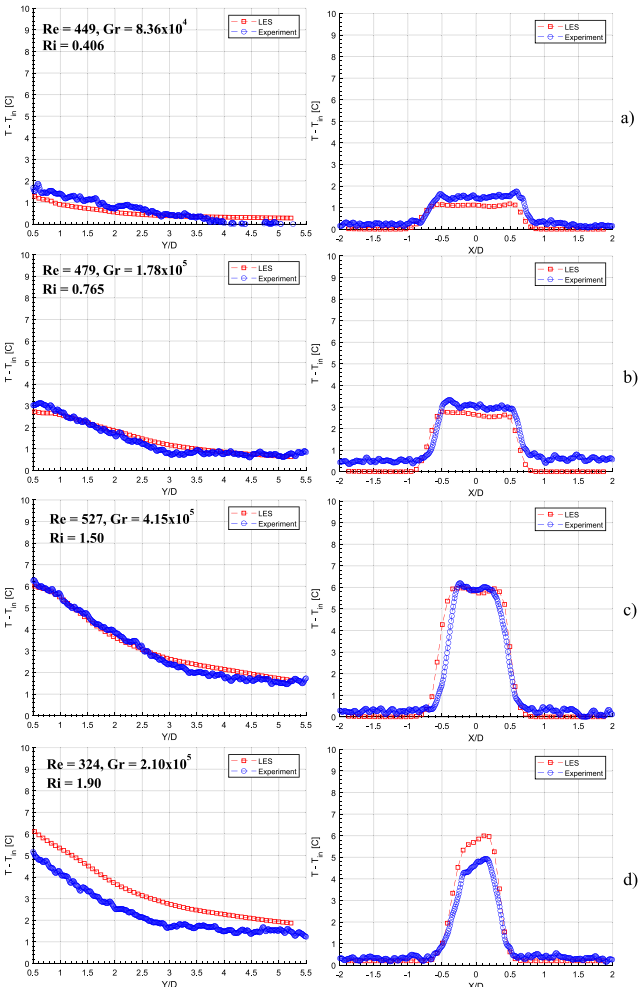


Fig. 15. Measured and predicted temperature profiles for the lines $X/D = 0$ (left) and $Y/D = 0.746$ (right) for a variety of conditions.

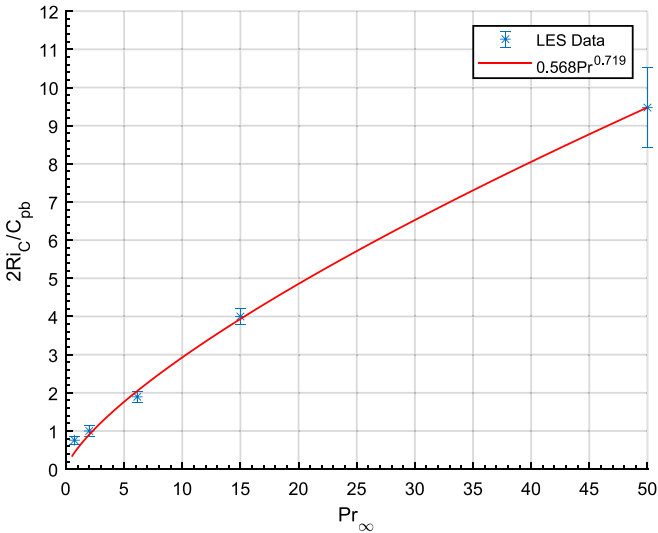


Fig. 16. Critical Ri versus Pr from LES simulations.

identified on Fig. 18, with improvement most notable for the VKV to EP regime and a general reduction in any systematic over/under prediction. This correction doesn't significantly change the predictions of the model for other, low-inlet-turbulence, studies so that the results remain

accurate for those cases. The effect of turbulent intensity on these regime transitions was not able to be studied experimentally due to the limitations on the inlet condition in this study. As such, it is recommended that equations (8)-(9) be examined in future experimental studies to determine if a better form exists, or if these simple relations remain sufficient.

$$Ri_{C1} = Ri_{T1}(1 + T_i) \quad (8)$$

$$Ri_{C2} = Ri_{T2}(1 + T_i) \quad (9)$$

5.4. Performance of transition criteria

To test Ri_{C2} , Table 4 shows the level of agreement between the predictions from the correlation to experimental data currently available for upward flow. Given the limited experimental data, the use of visual observations and the relatively coarse bounds of Ri_C in the LES simulations the criteria performs well, generally classifying regimes within error as shown in Fig. 18. Furthermore, it predicts the transitions in the only other relevant study in this configuration. Finally, the model predicts the regime transitions accurately for the synthetic data generated using LES for all tested parametric variations in Pr . These criteria offer the ability to predict flow topology for a wide range of working conditions. The shaded regions represent the approximate zone over which the transitions cover. This was chosen to cover the data points most difficult to visually identify. This is to account for both the subjective nature of visual observations and that transitions are in reality less abrupt than an absolute criteria would suggest.

6. Model implications

The curve fit presented on Fig. 16 while strong, has its largest error for $Pr = 0.7$. While it is possible that this could be improved upon by adding additional points to the fit, or by changing to a different functional form it is currently believed that this may be a sign of a different triggering mechanism for Ri_{C2} , as discussed in section 6.2.

The best modelling approach moving forward likely would be to generate a piece-wise formulation wherein cases at low Pr are predicted using a different formalism than cases with higher Pr . The natural dividing line between these two behaviours would appear to be $Pr = 1$, where the thermal and momentum boundary layer thicknesses are equal. This would require additional experimental and simulation campaigns to add additional data to Fig. 16.

Additionally, the shape of the curve generated on Fig. 16 for Pr approaching zero would seem to suggest that a third distinct regime may exist for fluids such as liquid metals. Hence the piece-wise approach may consider a third set of transition criteria for such flows. With this in mind, experimental and simulation studies expanding these criteria from $0.01 < Pr < 0.7$ would be of great interest to extend this work.

7. Conclusion

Fluid temperature and velocity measurements from a cylinder in mixed convection flows were presented and examined. A strong dependency of the flow topology behind the cylinder on the inlet velocity and heater power was found. Three distinct flow regimes were identified and used to create a flow regime map. This flow regime map was then divided by transition criteria developed and found to identify the regimes well, with some outliers near transition points.

LES simulations were performed and validated against the experimental data obtained. The performance of the LES model was generally good with RMS error largely agreeing with experimental data to within measurement uncertainty for velocity and temperature predictions respectively. The LES model was found to tend to over predict the velocity and fluid temperature as Ri increased and the conditions became more buoyant.

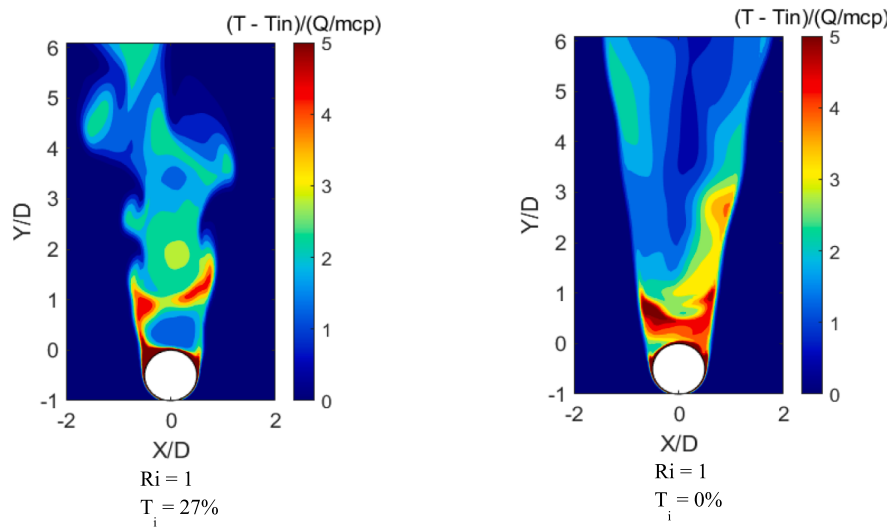


Fig. 17. Instantaneous non-dimensional temperature profiles with (left) and without (right) the inlet turbulent intensity at conditions of $Re = 554$, $Gr = 4.77 \times 10^5$.

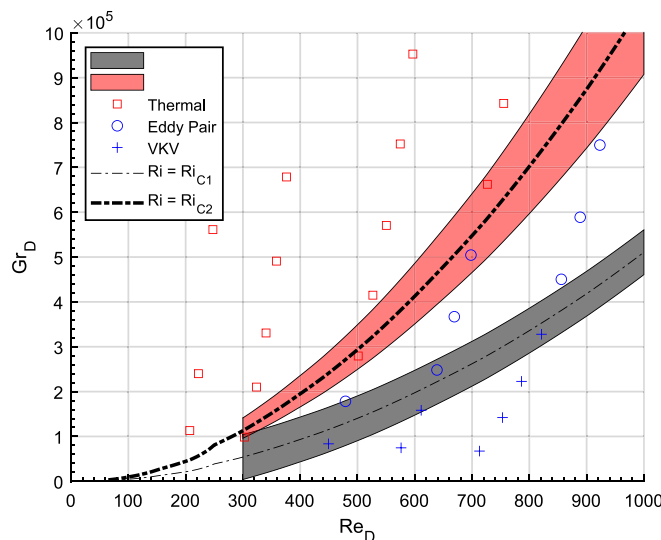


Fig. 18. Flow regime map with proposed transition criteria. The shaded regions are derived based on experimental uncertainty in the identification of the regime transitions and are intended to illustrate that the transitions occur gradually across these regions.

Table 4

Performance of the transition criteria from experiments conducted in this work and Singh et al. (2007).

Study	Re	C_{pb}	Inlet T_i (%)	Pr_∞	Ric_{exp}	Ric_{prea}
Singh et al., 2007	94	0.68	N/A	0.73	0.122	0.154
Singh et al., 2007	110	0.75	N/A	0.73	0.157	0.170
Present	414	0.95	27	6.13	0.92 ± 0.2	1.25
Present	590	0.90	30	6.13	1.15 ± 0.1	1.18

Flow regime transition criteria was identified as a function of Ri and proposed to handle the destruction of pure von Karman vortices, the beginning of a symmetric shedding mode and the removal of all vortex generation. The symmetric shedding mode was found to be analogous to isothermal slit experiments which split the re-circulation zone with momentum forces instead of buoyancy. Additionally, a strong dependency on the thermal boundary layer thickness or Pr was found for the removal of all vortex generation with a functional form proposed

based on LES simulations. This was found to agree well with the limited data available in literature, the new data collected in this paper, and the set of LES simulations performed over a wide range of conditions. The Pr dependency in part explains the significant differences between the critical Ri measured for water and air experiments in existing literature with mechanisms postulated.

CRediT authorship contribution statement

C.W. Hollingshead: Validation, Software, Formal analysis, Data curation, Writing – original draft, Writing – review & editing, Visualization, Project administration. **A. Rashkovan:** Methodology, Visualization, Resources, Writing – review & editing. **D.R. Novog:** Conceptualization, Methodology, Resources, Writing – review & editing, Supervision, Project administration, Funding acquisition.

Declaration of Competing Interest

The authors declare the following financial interests/personal relationships which may be considered as potential competing interests: David Novog reports financial support was provided by University Network of Excellence in Nuclear Engineering. David Novog reports financial support was provided by National Sciences and Engineering Research Council of Canada.

Data availability

Data will be made available on request.

Acknowledgements

This paper would not have been possible without the generous financial support of the NSERC Industrial Research Chair program and the University Network of Excellence in Nuclear Engineering (UNENE).

References

- Aarnes, J.R., Andersson, H.I., Haugen, N.E.L., 2018. Numerical investigation of free-stream turbulence effects on the transition-in-wake state of flow past a circular cylinder. *Journal of Turbulence* 19, 252–273.
- Achenbach, E., 1968. Distribution of local pressure and skin friction around a circular cylinder in cross-flow up to $Re=5 \times 10^6$. *Journal of Fluid Mechanics* 34, 625–639.
- Baek, H., Karniadakis, G.E., 2009. Suppressing vortex-induced vibrations via passive means. *Journal of Fluids and Structures* 25, 848–866.
- Celik, I., Cehreli, Z.N., Yavuz, I., 2005. Index of Resolution Quality for Large Eddy Simulations. *Journal of Fluids Engineering* 127, 949–958.

- Cengel, Y.A., 2002. Combined Natural and Forced Convection. In: HeAt TrAnsfer. A PrActicAl ApproAch. McGraw-Hill, pp. 486–501.
- Chang, K.S., Sa, J.Y., 1990. The effect of buoyancy on vortex shedding in the near wake of a circular cylinder. *Journal of Fluid Mechanics* 220, 253–266.
- Clifford, C.E., Kimber, M.K., 2020. Assessment of RANS and LES turbulence models for natural convection in a differentially heated square cavity. *Numerical Heat Transfer, Part A: Applications* 78, 560–594.
- Feng, L.H., Wang, J.J., 2010. Circular Cylinder vortex-synchronization control with a synthetic jet positioned at the rear stagnation point. *Journal of Fluid Mechanics* 662, 232–259.
- Fu, H., Rockwell, D., 2005. Shallow flow past a cylinder: control of the near wake. *Journal of Fluid Mechanics* 539, 1–24.
- Gandikota, G., Amirouidine, S., Chatterjee, D., Biswas, G., 2010. The Effect of Aiding/ Opposing Buoyancy on Two Dimensional Laminar Flow Across a Circular Cylinder. *Numerical Heat Transfer, Part A: Applications* 58, 385–402.
- Gao, D.L., Chen, W.L., Li, H., Hu, H., 2017. Flow around a circular cylinder with slit. *Experimental Thermal and Fluid Science* 82, 287–301.
- Hollingshead, C.W., Rashkovian, A., Novog, D.R., 2022. Mixed convection around two vertically aligned horizontal cylinders: A numerical, experimental, and modeling investigation on the effect of local conditions on heat transfer. *Nuclear Engineering and Design* 394.
- Hu, H., Koochesfahani, M.M., 2011. Thermal effects on the wake of a heated circular cylinder operating in mixed convection regime. *Journal of Fluid Mechanics* 685, 235–270.
- Kakade, A.A., Singh, S.K., Panigrahi, P.K., Muralidhar, K., 2010. Schlieren investigation of the square cylinder wake: Joint influence of buoyancy and orientation. *Physics of Fluids* 22.
- Khashechi, M., Abdi, I.A., Hooman, K., 2015. Characteristics of the wake behind a heated cylinder in relatively high Reynolds number. *International Journal of Heat and Mass Transfer* 86, 589–599.
- Lecordier, J.C., Hamma, L., Paranthoen, P., 1991. The control of vortex shedding behind heated circular cylinders at low Reynolds numbers. *Experiments in Fluids* 10, 224–229.
- Lecordier, J.C., Browne, L.W.B., Masson, S., Dumouchel, F., Paranthoen, P., 2000. Control of vortex shedding by thermal effects at low Reynolds number. *Experimental Thermal and Fluid Sciences* 21, 227–237.
- Ma, H., He, L., 2021. Large Eddy simulation of natural convection heat transfer and fluid flow around a horizontal cylinder. *International Journal of Thermal Sciences* no. 162.
- Michaux-Leblond, N., Belorgey, M., 1997. Near-Wake Behaviour of a Heated Circular Cylinder: Viscosity-Buoyancy Duality. *Experimental Thermal and Fluid Science* 15, 91–100.
- Norberg, C., 1994. An Experimental investigation of the flow around a circular cylinder: influence of aspect ratio. *Journal of Fluid Mechanics* 258, 287–316.
- Rajani, B.N., Kandasamy, A., Majumdar, S., 2009. Numerical simulation of laminar flow past a circular cylinder. *Applied Mathematic Modelling* 33, 1228–1247.
- Rajani, B.N., Kandasamy, A., Majumdar, S., 2016. LES of Flow past Circular Cylinder at $Re = 3900$. *Journal of Applied Fluid Mechanics* 9, 1421–1435.
- Shi, X., Feng, L., 2015. Control of flow around a circular cylinder by bleed near the separation points. *Experiments in Fluids* 214.
- Singh, S., Chandar, D., 2016. Effects of thermal induced buoyancy forces on the vortex shedding of a circular cylinder. *International Communications in Heat and Mass Transfer* 76, 215–224.
- Singh, S., Biswas, G., Mukhopadhyay, A., 1998. Effect of Thermal Buoyancy on the Flow Through a Vertical Channel with a Built-In Circular Cylinder. *Numerical Heat Transfer, Part A* 769–789.
- Singh, S.K., Panigrahi, P.K., Muralidhar, K., 2007. Effect of buoyancy on the wakes of circular and square cylinders: a schlieren-interferometric study. *Experiments in Fluids* 43, 101–123.
- Wan, H., Patnaik, S.S., 2016. Suppression of vortex-induced vibration of a circular cylinder using thermal effects. *Physics of Fluids* 28.
- Williamson, C., Roshko, A., 1990. Measurements of base pressure in the wake of a cylinder at low Reynolds numbers. *Z. Flugwiss. Weltraumforschung* 14, 38–46.
- L. Xiyun, L.Guocan, 2002. “A Large Eddy Simulation of the Near Wake of a Circular Cylinder.” *Chinese Journal of Mechanics*.
- M.M. Zdravkovich. *Flow around circular cylinders Vol 1: Fundamentals*, Oxford University Press Inc. 1997.